*J. Fluid Mech.* (2021), *vol*. 911, A8, doi:10.1017/jfm.2020.1017

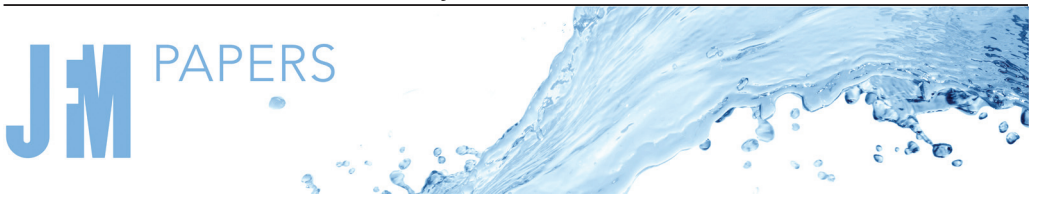

# Ubiquity of particle–vortex interactions in turbulent counterflow of superfluid helium

**P. Švančara[1], D. Duda[1,‡], P. Hrubcová[1,§], M. Rotter[1], L. Skrbek[1], M. La Mantia[1,†], E. Durozoy[2], P. Diribarne[3], B. Rousset[3], M. Bourgoin[4] and M. Gibert[2]**

[1]Faculty of Mathematics and Physics, Charles University, Ke Karlovu 3, 121 16 Prague, Czech Republic

[2]Univ. Grenoble Alpes, CNRS, Grenoble INP, Institut Néel, 38000 Grenoble, France

[3]Univ. Grenoble Alpes, CEA IRIG-DSBT, 38000 Grenoble, France

[4]Laboratoire de Physique, Université Lyon, ENS de Lyon, Université Lyon 1, CNRS, 69342 Lyon, France

(Received 16 April 2020; revised 14 October 2020; accepted 9 November 2020)

Thermal counterflow of superfluid $^4$He is investigated experimentally, by employing the particle tracking velocimetry technique. A flat heater, located at the bottom of a vertical channel of square cross-section, is used to generate this unique type of thermally driven flow. Micronic solid particles, made *in situ*, probe this quantum flow and their time-dependent positions are collected by a digital camera, in a plane perpendicular to the heat source, away from the channel walls. The experiments are performed at relatively large heating powers, resulting in fluid velocities exceeding 10 mm s$^{-1}$, to ensure the existence of sufficiently dense tangles of quantized vortices. Within the investigated parameter range, we observe that the particles intermittently switch between two distinct motion regimes, along their trajectories, that is, a single particle can experience both regimes while travelling upward. The regimes can be loosely associated with fast particles, which are moving away from the heat source along almost straight tracks, and to slow particles, whose erratic upward motion can be said to be significantly influenced by quantized vortices. We propose a separation scheme to study the properties of these regimes and of the corresponding transients between them. We find that particles in both regimes display non-classical, broad distributions of velocity, which indicate the relevance of particle–vortex interactions in both cases. At the same time, we observe that the fast

† Email address for correspondence: lamantia@mbox.troja.mff.cuni.cz
‡ Present address: Faculty of Mechanical Engineering, University of West Bohemia, Plzeň, Czech Republic.
§ Present address: Department of Physics, Royal Holloway University of London, Egham, Surrey, United Kingdom.

particles move along straighter trajectories than the slow ones, suggesting that the strength of particle–vortex interactions in the two regimes is notably different.

**Key words:** quantum fluids, particle/fluid flow, turbulent flows

## 1. Introduction

The superfluid phase of liquid $^4$He is often called He II and can be regarded as an easily accessible quantum fluid, compared with other systems, such as superfluid $^3$He (see, for example, Barenghi, Skrbek & Sreenivasan 2014; Mongiovì, Jou & Sciacca 2018). He II is usually obtained from the normal liquid phase, known as He I, by evaporative cooling below the transition temperature $T_\lambda$, equal to 2.17 K at the saturated vapour pressure, and its extraordinary physical properties, such as the extremely small kinematic viscosity, allow the study of highly turbulent flows in relatively compact set-ups (Skrbek & Sreenivasan 2012).

The most popular phenomenological description of the large-scale hydrodynamics of He II postulates that the liquid consists of two components, with temperature-dependent relative densities (Barenghi *et al.* 2014). In the close proximity of $T_\lambda$, He II is made solely of the normal component, which behaves similarly to a classical fluid possessing finite viscosity. As the temperature decreases, the corresponding relative density decreases and the superfluid component – inviscid and of zero entropy – becomes more abundant. Eventually, below 1 K, He II can be, for many practical purposes, regarded as a pure superfluid.

Additionally, it follows from the quantum mechanical description of He II that the flow of the superfluid component is potential. Yet vortical flows may occur in this unique system due to the presence of quantized vortices, which are one-dimensional topological defects – holes – within the superfluid component. The core size of these vortex lines is of the order of 0.1 nm and their circulation quantum $\kappa$ is equal to $h/m_4 \approx 10^{-7}$ m$^2$ s$^{-1}$, where $h$ is the Planck constant and $m_4$ denotes the mass of the $^4$He atom. Typically, these vortices arrange themselves in a dynamic tangle, interacting with the fluid flow via the mutual friction force, and represent the main ingredient of what is usually called quantum turbulence. A relevant intensity measure of quantum turbulence then becomes the vortex line density $L$, defined as the total length of quantized vortex lines per unit volume.

When heat is dissipated in He II, the fluid is set into motion and, in the standard semiclosed channel geometry, with the heat source located at the closed end, the normal component flows away from the heater. In the steady state, the normal component will flow, on average, at a constant velocity, whose magnitude $v_n$ can be written as

$$v_n = \frac{q}{\rho S T}, \tag{1.1}$$

where $q$ denotes the applied heat flux, $\rho$ is the He II density, $S$ indicates the fluid specific entropy and $T$ is the liquid temperature. The superfluid component flows in the opposite direction, i.e. toward the heater, with the average velocity magnitude $v_s$, in such a way that the net mass flow equals zero, that is, $\rho_n \boldsymbol{v}_n + \rho_s \boldsymbol{v}_s = 0$, where the subscripts $n$ and $s$ denote the normal and superfluid components, respectively. This flow, called thermal counterflow, has no direct classical analogue, especially if one considers that the liquid is characterized by an extremely large thermal conductivity, which actually depends on the heat flux (Mongiovì *et al.* 2018). The magnitude of the flow characteristic velocity, which

is called the counterflow velocity $v_{ns}$, is defined as

$$v_{ns} = |\boldsymbol{v}_n - \boldsymbol{v}_s| = \frac{q}{\rho_s S T}. \tag{1.2}$$

Channel counterflow represents the hallmark of both experimental and numerical studies of quantum turbulence (Skrbek & Sreenivasan 2012). Here, we investigate its properties experimentally, by flow visualization. Specifically, we observe the motions of relatively small solid particles dispersed in the liquid, which proved their usefulness as probes of both classical and quantum features of He II flows (Guo *et al.* 2014). Indeed, the interactions between flow-probing particles and quantized vortices can be observed as events of extremely large particle velocity and it has been shown that the corresponding statistical distributions display power-law tails at sufficiently small scales (La Mantia *et al.* 2016).

In order to appreciate the latter remark, two principal scales are introduced. The smallest, experimentally resolved scale, which we call here the scale $s_p$ probed by the particles, is defined as the mean particle displacement between two consecutive positions and can be written as

$$s_p = \langle v \rangle \, t_p, \tag{1.3}$$

where $\langle v \rangle$ is the mean particle velocity, obtained at the corresponding time scale $t_p$ (the typical particle size is usually smaller than or of the same order of $s_p$). The characteristic scale of the flow, which we call here the quantum scale $s_q$, is the mean distance between quantized vortices. The latter can be obtained from the flow vortex line density – as discussed, for example, by Sergeev, Barenghi & Kivotides (2006) – because, at large enough $v_{ns}$, in the steady state, one can write

$$s_q = \frac{1}{\sqrt{L}} = \frac{1}{\gamma v_{ns}}, \tag{1.4}$$

where $\gamma$ is an empirical scaling constant depending not only on the liquid temperature (Babuin *et al.* 2012) but also on the channel geometry (Hrubcová, Švančara & La Mantia 2018), that is, on how close the channel boundaries are to the investigated flow region.

If the experimental resolution falls significantly behind the quantum scale, that is, if the probed scale $s_p$ is appreciably smaller than the mean distance $s_q$ between quantized vortices, the tails of the particle velocity statistical distribution are clearly visible, with distinctive power-law scaling (La Mantia *et al.* 2016). As the probed scale increases, the tails become less visible, but are still noticeable, and, when $s_p > s_q$, the tails disappear and we observe that the particle velocity distribution shape is almost Gaussian, resembling therefore classical turbulence (Švančara & La Mantia 2017) and indicating the averaged result of multiple interactions between particles and quantized vortices (Švančara & La Mantia 2019).

To date, distinctive motion features have been observed in experiments involving particles probing thermal counterflow in vertical channels, with the heat source located at the channel bottom. At relatively small heat fluxes, a significant number of particles move, on average, toward the heater (Paoletti *et al.* 2008; La Mantia 2016), that is, downward, in the direction of the superfluid component. As $q$ increases, the portion of particles moving upward, away from the heater, in the normal fluid direction, increases, indicating that, at relatively large heat fluxes, the particles tend to follow, on average, the normal fluid flow, although the corresponding tracks become less straight than at smaller $q$ values (La Mantia 2016). Additionally, it was found that the mean particle velocity in the counterflow direction is approximately equal to $v_n$ (Paoletti *et al.* 2008; Chagovets & Van Sciver 2011)

or to $v_n/2$ (Zhang & Van Sciver 2005; Chagovets & Van Sciver 2011), with the latter occurring at larger heat fluxes – a similar decrease of the mean particle velocity was obtained in numerical simulations and attributed to the stronger interactions between particles and quantized vortices at larger $L$ values (Kivotides 2008*a*).

Recently, Mastracci & Guo (2018) further investigated the occurrence of these particle motion features, by using a square channel of 16 mm sides, and confirmed the above-mentioned experimental findings. Additionally, they found that, at the largest $q$ values probed in their experiments, the statistical distributions of the particle velocity in the vertical direction (i.e. the normal fluid direction) are characterized by a single peak centred near $v_n/2$. As the applied heat flux decreases, another peak, centred near $v_n$, appears in these velocity distributions and, for even smaller $q$ values, the peak at the smaller velocity is centred near $v_s$, which is taken with the negative sign, as the superfluid and normal fluid components move in opposite directions. The outcome indicates that, at small heat fluxes, particles can be trapped onto quantized vortices for relatively long times and move therefore downward, in the superflow direction, with the vortex tangle – see, e.g. Sergeev & Barenghi (2009) for a discussion on particle trapping. For larger $v_{ns}$ values, the Stokes drag of the normal component forces instead most particles to move upward, away from the heater, that is, the probes tend to stay trapped onto vortices for shorter times.

In this work, we focus on the intermediate range of counterflow velocity, occurring when the vast majority of particles move upward, in the normal fluid direction, away from the heat source, with the corresponding streamwise (vertical) velocity distributions characterized by two peaks centred near $v_n/2$ and $v_n$. We specifically observe frequent velocity changes along individual particle trajectories and, as detailed below, we propose a separation scheme that allows us to neatly identify two motion regimes. Our results clearly show that the flow-induced motion of single particles can be associated with the low velocity peak of the velocity distribution, when it can be said that the particle motion is significantly influenced by quantized vortices (slow regime), or to the high velocity peak, when it appears that the particle motion is greatly affected by the imposed normal fluid velocity (fast regime).

However, before proceeding, it is important to remark that a direct, quantitative comparison between our results and those reported by Mastracci & Guo (2018) is currently not possible because our square channel is larger (it has 25 mm sides) and, as discussed, for example, by Babuin *et al.* (2012), the transition to the turbulent state occurs at smaller fluid velocities in larger channels – see also La Mantia (2016). It follows that in our channel a single-peaked velocity distribution can be obtained at $q$ values corresponding to double-peaked distributions in the channel used by Mastracci & Guo (2018). Additionally, in the latter case, the investigated flow region included the channel walls, where quantized vortices tend to preferentially concentrate, as discussed, for example, by Baggaley & Laizet (2013) and La Mantia (2017), while the present results are obtained away from the walls, in the channel bulk region, but also at a distance from the heat source smaller than in the case reported by Mastracci & Guo (2018) – see, e.g. Bertolaccini, Lévêque & Roche (2017) and Švančara *et al.* (2018*b*) for discussions on the role of the entrance length in thermal counterflow. Consequently, at the same heat flux, the actual $L$ values of the regions experimentally probed are not expected to be equal. On the other hand, the features of particle motion introduced above have been identified in both channels, although at different $q$ values, indicating therefore that their occurrence is not qualitatively influenced by the flow geometry.

More importantly, we show here that the interactions between quantized vortices and flow-probing particles appear to be relevant not only for the slow particles, as claimed in the past, for example, by Mastracci & Guo (2018), but also for the fast ones, at least in the

range of investigated parameters, that is, for sufficiently dense vortex tangles, in turbulent counterflow. Specifically, we find that both slow and fast particles display non-classical, broad distributions of velocity, which are characterized by heavy tails and indicate the occurrence of particle–vortex interactions in both regimes. This can be regarded as the work's main scientific result, obtained by applying the just mentioned separation scheme.

The paper is organized as follows. In § 2 we describe our visualization set-up and in § 3.1 we use the statistical distributions of the streamwise particle velocity to estimate the normal fluid velocity for our experiments. We then show how the different velocity regimes of particle motion can be separated (§ 3.2) and investigate their properties (§§ 3.3–3.6), before concluding in § 4.

## 2. Methods

The Prague cryogenic visualization set-up was employed for data acquisition – see, e.g. Švančara *et al.* (2018*b*) and references therein for detailed descriptions. In brief, it consists of a low-loss helium cryostat with the experimental volume located at its bottom; the latter has a square cross-section, of 51 mm sides, and is 300 mm high. The optical access to the volume is provided by multilayered windows, of 25 mm diameter, located 100 mm above the volume bottom, in the middle of each side. Two windows are used for the laser sheet (approximately 10 mm high and 1 mm thick) and one for the camera.

Thermal counterflow is investigated in a semiclosed glass channel of square cross-section, see figure 1, vertically mounted inside the experimental volume. The flow source is a planar resistive heater located at the bottom of the channel. As mentioned above, when the heater is switched on, the normal component flows upward, i.e. in the positive vertical direction, while the superfluid component flows toward the heater.

We seed liquid helium with solid deuterium particles in order to visualize its flow. The particles are made *in situ* by abrupt solidification from the gaseous phase (approximately 2 % of deuterium gas diluted into helium gas is introduced into the bath by several short pulses). We capture the particle motions by using a CMOS camera, sharply focused on the plane illuminated by the laser sheet. The camera field of view (FOV) is 13 mm × 8 mm, with 1 megapixel spatial resolution.

Each acquired movie is characterized by the temperature $T$ of the He II bath, the heat flux $q$ supplied by the heater and the camera frame rate $f$, and consists of hundreds of frames (up to a few thousands). In order to obtain large data sets, we collected between five and 105 movies for each experimental condition. Individual camera frames were processed by employing a custom-made tracking algorithm, providing sets of particle positions linked to the respective trajectories. Raw tracks were smoothed and differentiated to obtain time-dependent velocities and accelerations.

Following Mordant, Crawford & Bodenschatz (2004), we estimated the particle velocities and accelerations by convolving their positions with Gaussian kernels, denoted below as $G_1$ and $G_2$, which are obtained as time derivatives of the Gaussian filter $G_0$, employed to smooth the trajectories. From $G_0(t) \sim \exp[-(t/\alpha\tau)^2]$ we obtain, for the particle velocities, $G_1(t) \sim -(t/\alpha\tau)G_0(t)$ and, for their accelerations, $G_2(t) \sim [2(t/\alpha\tau)^2 - 1]G_0(t)$, where $t$ indicates the time and $\tau = 1/f$ (the relations are only proportional because the kernels have to be adequately normalized).

The non-dimensional parameter $\alpha$ controls the level of smoothing and here we use 1.7 for $G_0$ and $G_1$, and 5.0 for $G_2$. We specifically studied the influence of this parameter on the standard deviations of the particle velocity and acceleration, and chose the $\alpha$ values resulting in relatively small standard deviation changes, following a procedure analogous

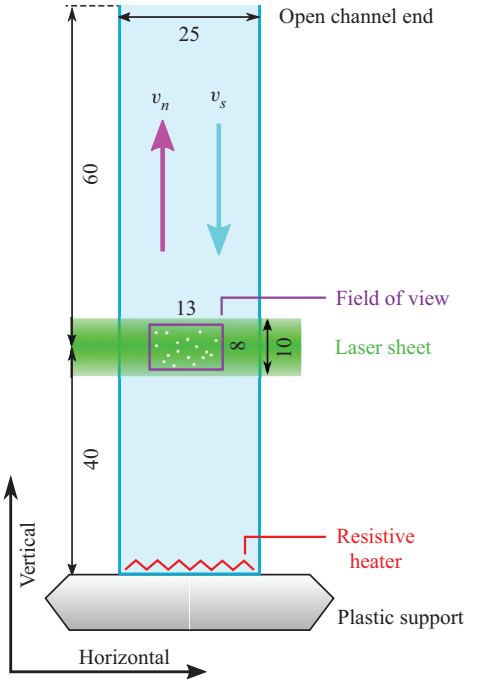


Figure 1. Schematic view of the channel, see La Mantia (2016) for a relevant picture; dimensions are in millimetres. The glass channel (light blue) has a square cross-section and its top is open to the surrounding helium bath. The channel glass walls are mounted on a frame and touch each other at the channel corners. The frame bottom (shaded grey) is slightly smaller than the experimental volume cross-section and the heater is located in its middle, inside the channel. The laser sheet (green) is approximately 1 mm thick (in the direction perpendicular to the scheme). The magenta and cyan arrows indicate the directions of the normal fluid velocity $\boldsymbol{v}_n$ and of the superfluid velocity $\boldsymbol{v}_s$, respectively. The horizontal and vertical directions used in the text are marked by black arrows.

to that outlined by Švančara, Hrubcová & La Mantia (2018*a*). Similarly, the convolution with discretely sampled positions was carried out in a finite sliding time window of width $2\beta\tau$, that is

$$x_i(t) = \sum_{t'=t-\beta\tau}^{t+\beta\tau} x(t')G_i(t'-t), \tag{2.1}$$

where $x_i$, with $i \in \{0, 1, 2\}$, indicates the position, velocity and acceleration, respectively, and $x$ denotes the raw position obtained from the tracking software; we set the parameter $\beta$ equal to 3 for particle positions and velocities, and to 10 for accelerations, that is, $\beta > \alpha$.

The finite width of the kernels is linked to the loss of time resolution because multiple raw positions are taken into account to obtain a smooth single position (velocity, acceleration). We can estimate the effective time resolution of the kernels to be $\tau' \approx 2\sqrt{2}\alpha\tau$, which is analogous to the 95% (two-sigma) confidence interval of the normal distribution. For the velocity estimate we obtain $\tau_1' \approx 5\tau$ and, in the case of the particle accelerations, $\tau_2' \approx 14\tau$.

It then follows that the latter time resolutions can be used in (1.3) as the characteristic time scale $t_p$ needed for the estimation of the scale $s_p$ probed by our particles, which consequently can be influenced by the specific feature (velocity, acceleration) one is trying to measure. Note also that the choice of the $\alpha$ and $\beta$ parameters depends in general on the

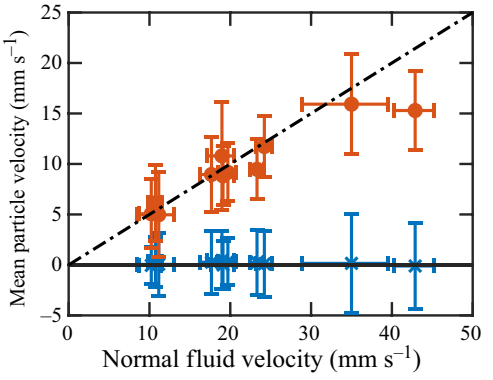


Figure 2. Mean horizontal (blue crosses) and vertical (red circles) particle velocities as a function of the normal fluid velocity $v_n$, computed from (1.1) by using the experimental volume cross-section (51 mm × 51 mm). Solid black line, null velocity; dot-dashed black line, $v_n/2$ scaling. The error bars correspond to the measurement standard deviation on the vertical axis and, on the horizontal axis, to the variation of $v_n$ due to the (relatively small) temperature changes occurring during each experimental run, associated with each point; results obtained from 11 data sets, containing at least 0.5 million velocity points each, are displayed in the figure.

experimental conditions and that here we chose values satisfying the standard deviation criterion mentioned above (Mordant *et al.* 2004; Švančara *et al.* 2018*a*).

## 3. Results and discussion

Experiments were carried out at temperatures ranging from 1.3 to 1.7 K. The temperature was kept constant by stabilizing the pressure of helium vapour (this was done by using a PC-controlled butterfly valve mounted between the cryostat and the pumping unit). To generate thermal counterflow, a power up to 2.5 W was applied to our planar heater. Since the walls and frame of our experimental channel are pressed against each other, we assume here, as in previous studies performed with the same set-up, that the applied heat leaks out of the channel and thermal counterflow occurs also outside the channel, within the experimental volume. Heat is therefore transported over an area larger than the channel cross-section and, as a first step, we set this area equal to the cross-section of our experimental volume (51 mm × 51 mm). It then follows from (1.1) that the corresponding range of normal fluid velocities is from 10 to 45 mm s$^{-1}$, which can therefore be regarded as a conservative estimate of the actual $v_n$ values. Note in passing that for the present channel the transition to the turbulent state was reported to occur for $v_{ns} \gtrsim 1$ mm s$^{-1}$ (La Mantia 2016).

Figure 2 displays the systematic dependence of the mean particle velocity on $v_n$ calculated from (1.1). We observe that the horizontal component (blue crosses) remains around zero, while the mean vertical velocity scales as $v_n/2$, up to approximately 25 mm s$^{-1}$, and deviates from this scaling for larger $v_n$ values. The outcome confirms therefore that the majority of our particles flow in the normal fluid direction, away from the heat source (see the above discussion on the features of particle motion in thermal counterflow).

The result also justifies, at least to a first approximation, our choice of assuming that the applied heat is transported over an area equal to that of the experimental volume cross-section because the mean particle velocity in the vertical direction scales as $v_n/2$ which is the value one would expect in the range of investigated parameters, that is,

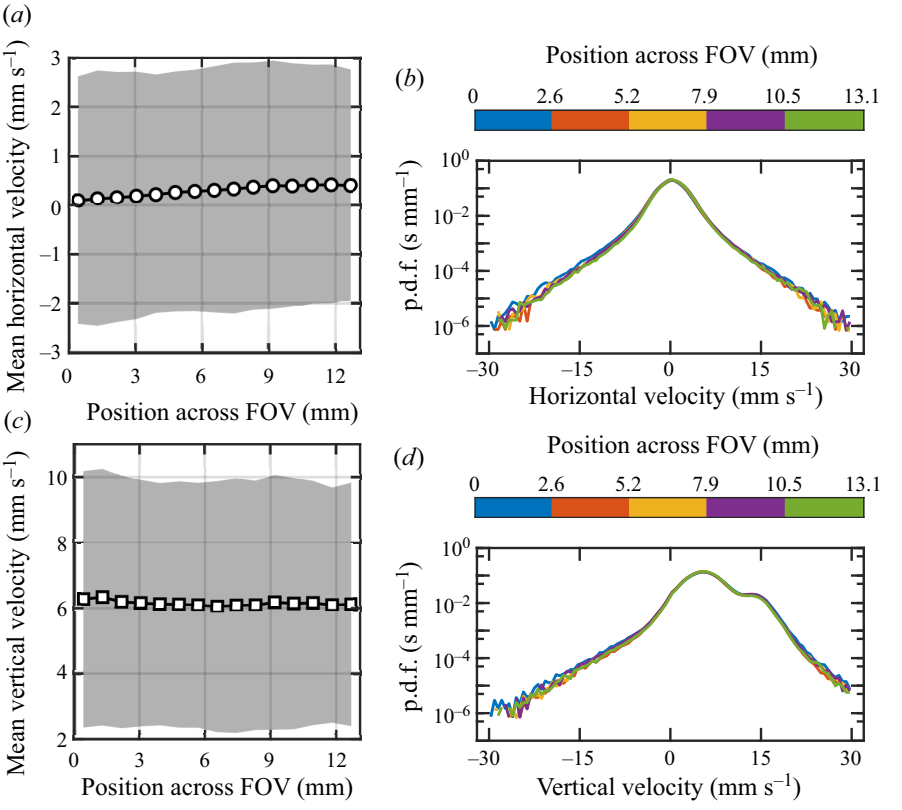


Figure 3. Uniformity of the particle velocity across the FOV. (*a*,*c*) Mean values of the horizontal (*a*, circles) and vertical (*c*, squares) velocities of the particles, calculated by splitting the FOV into 15 vertical regions; grey areas, corresponding velocity standard deviation. (*b*,*d*) Probability density functions (p.d.f.s) of the horizontal (*b*) and vertical (*d*) velocities of the particles, calculated by splitting the FOV into five vertical regions, indicated by the colour map. Data set collected at 1.36 K, with an applied heat power $P = 0.61$ W.

at sufficiently small values of heat flux – note in passing that the mean particle velocity can also be significantly smaller than $v_n/2$ in dense vortex tangles (Kivotides 2008*a*). Additionally, as discussed below, in § 3.5, particle trajectories do not show any prominent deviation from the vertical direction.

However, one cannot in principle exclude that inhomogeneous parasitic flows, due to the heat leak from the channel, may affect the observed particle dynamics. These flows may occur (i) in the close proximity of the heat source, where the channel walls are pressed against its bottom support, and (ii) at the corners where the vertical walls are pressed against each other, see figure 1. We also note that a small part of the heat supplied by the planar heater is conducted through the bottom structure to the bulk helium and convected by a counterflow around the channel, because the bottom structure temperature, due to the finite conductivity of the heater and support, and to Kapitza resistance, is always slightly higher than that of the surrounding liquid. Considering that our FOV – 13 mm × 8 mm – is located approximately 40 mm away from the heater, in the middle of the channel, of 25 mm sides, and approximately 14 mm away from the corners of the channel, along the corresponding diagonals, one may say that the FOV is relatively far away from the just mentioned problematic spots.

In order to quantitatively check if this is far enough, that is, in order to further justify our assumption that the applied heat is transported over an area larger than that of the channel cross-section, we divided the FOV into rectangular regions, and computed for each of them the mean particle velocity, in all probed experimental conditions. We found that the latter velocity is always directed upward, i.e. away from the heat source, with negligible side component and approximately constant magnitude, regardless of the number of regions in which the FOV is divided. Specifically, the mean value of the horizontal velocity is always close to zero and substantially smaller than the corresponding standard deviation (it is also much smaller than the mean value of the vertical velocity).

The outcome is shown explicitly in figure 3 for a large data set containing more than eight million particle positions, obtained at 1.36 K, with an applied heat power $P = 0.61$ W. Panels (*a*,*c*) display the particle velocity components as a function of the particle position across the FOV, split into 15 vertical regions. It can be seen that the mean horizontal velocity is slightly larger on the right-hand side of the FOV, but its magnitude is close to zero and much smaller than the corresponding standard deviation, plotted in the panel as the grey area (other data sets display similar features but with less evident systematic behaviour of the mean horizontal velocity). More importantly, relevant statistical distributions of the particle velocity, computed after splitting the FOV into five vertical regions, are plotted in panels (*b*,*d*) of the same figure and neatly overlap (the velocity statistical distributions of the particles are discussed below in detail). The latter result clearly demonstrates that the observed particle dynamics does not depend appreciably on the particle position within the FOV, that is, no evidence of significant parasitic flows is found in our data.

### 3.1. *Statistical distributions of the particle vertical velocity*

As mentioned above, the probability density functions (p.d.f.s) of the particle vertical velocity display either one or two local maxima. From now on we focus on three data sets that are characterized by two neat distribution maxima which are well separated from each other and centred near $v_n/2$ and $v_n$, that is, the vertical velocity distributions of the other data sets considered for figure 2 display only one prominent peak – see table 1 for relevant experimental conditions.

The first step of the analysis is to fit the vertical velocity distributions with a double-peaked Gaussian function, see figure 4(*a–c*). The fits neatly follow the experimental data in the distributions cores (the tails are discussed below) and the peak velocities, $v_1 < v_2$, with the respective standard deviations, $\sigma(v_1)$ and $\sigma(v_2)$, can be obtained from the fits. Following Mastracci & Guo (2018) the peak velocities are expected to scale as $v_1 = v_n/2 + v_{sl}$ and $v_2 = v_n + v_{sl}$, where $v_{sl}$ denotes the non-zero slip velocity due to the density difference between He II and solid deuterium – note that Mastracci & Guo (2018) set arbitrarily the $v_1$ offset to approximately 2 mm s$^{-1}$.

It then follows that $v_1$ and $v_2$ obey the scaling relation

$$2v_1 = v_2 + v_{sl}, \tag{3.1}$$

which allows us to verify the origin of the two peaks and to determine $v_{sl}$. We plot this dependence in figure 5 (circles), with a linear fit of unit slope (line). The scaling is clearly verified and we can hence estimate the slip velocity $v_{sl}$ to be approximately equal to $-2.5$ mm s$^{-1}$. The negative sign indicates that our particles are heavier than He II and, indeed, solid deuterium is heavier than He II.

| # | $T$ (K) | $P$ (W) | $f$ (f.p.s.) | $N$ ($10^6$) | $v_n$ (mm s$^{-1}$) | $v_{ns}$ (mm s$^{-1}$) |
|---|---|---|---|---|---|---|
| 1 | $1.39 \pm 0.02$ | 1.22 | 800 | 1.4 | 18.7 | 20.2 |
| 2 | $1.36 \pm 0.02$ | 0.61 | 800 | 8.6 | 10.9 | 11.6 |
| 3 | $1.52 \pm 0.03$ | 1.23 | 250 | 1.1 | 10.2 | 11.7 |

Table 1. Experimental conditions for the data sets displaying bimodal behaviour, see also figure 4: $T$, temperature of the He II bath; $P$, applied heat power; $f$, camera frame rate; $N$, number of particle positions in the data set; $v_n$, normal fluid velocity computed from (1.1) by using the experimental volume cross-section; $v_{ns}$, counterflow velocity computed from (1.2) by using the experimental volume cross-section. Note that the velocity values reported here can be regarded as conservative estimates of the actual values, see the text for details.

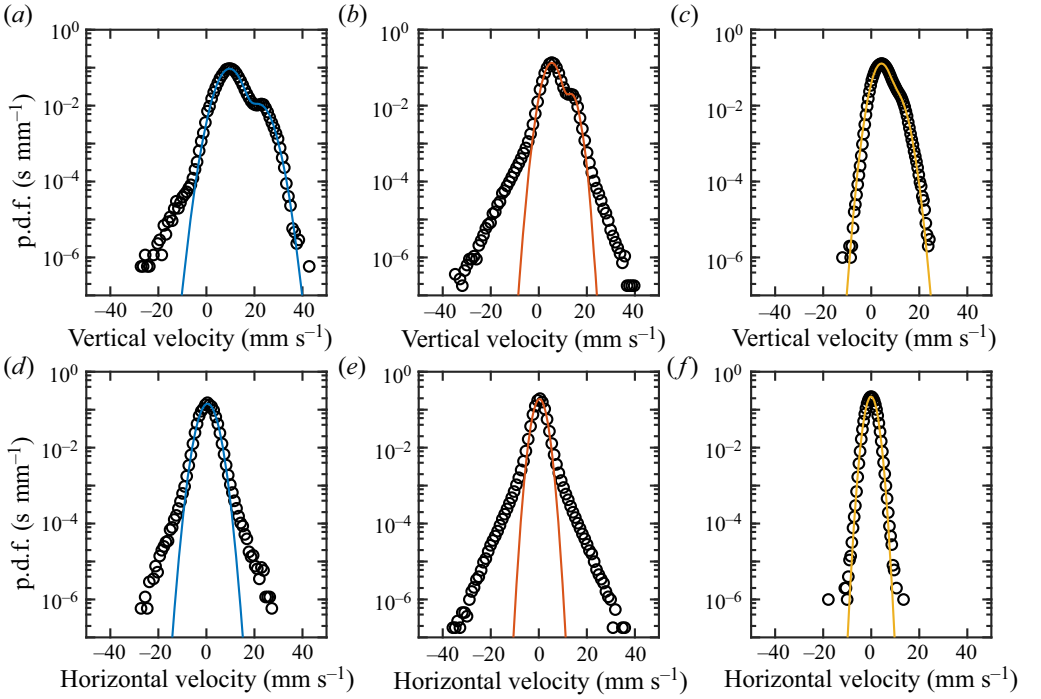


Figure 4. The p.d.f.s of the particle velocities. (*a–c*) Distributions of the vertical component (black circles) with their double-peaked Gaussian fits (colour lines). (*d–f*) Distributions of the horizontal component with their single-peaked Gaussian fits. Panels (*a*,*d*), (*b*,*e*) and (*c*,*f*) correspond to data sets #1, #2 and #3, respectively, see table 1 for relevant experimental conditions.

If we assume that $v_{sl}$ is equal to the terminal velocity of a freely falling spherical particle, we can estimate the corresponding particle radius $r$ from Stokes' formula

$$r = \sqrt{\frac{9}{2}\frac{\mu v_{sl}}{g(\rho_p - \rho)}}, \tag{3.2}$$

where $\mu$ and $\rho$ denote the temperature-dependent dynamic viscosity and density of He II, respectively, tabulated by Donnelly & Barenghi (1998), $g$ indicates the acceleration due to gravity and $\rho_p = 200\ \mathrm{kg\,m^{-3}}$ is the density of solid deuterium, estimated from its crystal structure (Bostanjoglo & Kleinschmidt 1967). For $T = 1.40$ K, we obtain $r \approx 5\ \mu$m, which

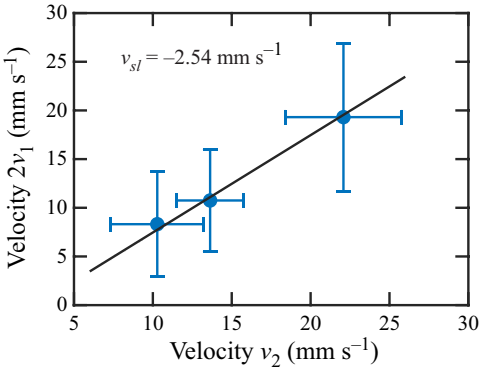


Figure 5. Scaling of the peak velocities, obtained from double-peaked Gaussian fits of the considered vertical velocity p.d.f.s. Blue circles, experimental data; see table 1 for relevant experimental conditions. The error bars indicate the standard deviation of the velocities. Black line, (3.1) with $v_{sl} = -2.54$ mm s$^{-1}$.

| # | $v_n$ (mm s$^{-1}$) | $v_s$ (mm s$^{-1}$) | $v_{ns}$ (mm s$^{-1}$) | $s_q$ (μm) | $s_p$ (μm) | $R$ |
|---|---|---|---|---|---|---|
| 1 | 24.6 | 1.9 | 26.5 | 35 | 70 | 2.0 |
| 2 | 16.2 | 1.1 | 17.3 | 58 | 45 | 0.8 |
| 3 | 12.8 | 1.9 | 14.7 | 48 | 110 | 2.3 |

Table 2. Characteristic flow velocities and scales, estimated from the slip and peak velocities, see the text for details; $v_n = v_2 - v_{sl} = 2(v_1 - v_{sl})$, normal fluid velocity magnitude, see also (3.1); $v_s = v_n\rho_n/\rho_s$, superfluid velocity magnitude; $v_{ns} = v_n + v_s$, counterflow velocity magnitude, see also (1.2); note that the velocity values reported here are larger than those listed in table 1; $s_q$, mean distance between quantized vortices, (1.4), note that relevant $\gamma$ values were obtained as discussed by Švančara *et al.* (2018*b*); $s_p$, scale probed by the particles, (1.3) with $t_p = 5/f$; $R = s_p/s_q$, non-dimensional scale ratio.

agrees with the typical size of the used particles – see, for example, Švančara & La Mantia (2017).

It is consequently possible to compute the normal fluid velocity $v_n$, the superfluid velocity $v_s$ and the counterflow velocity $v_{ns}$ following the procedure just outlined – see table 2 for relevant results. Specifically, we set the normal fluid velocity magnitude $v_n$ equal to $v_2 - v_{sl} = 2(v_1 - v_{sl})$, by using (3.1) and the corresponding values of peak and slip velocities, estimated from the probability density functions of the particle vertical velocity. We then take into account that, in thermal counterflow, the mass flow rate is null and, consequently, we set the superfluid velocity magnitude $v_s$ equal to $v_n\rho_n/\rho_s$, where, as mentioned above, the fluid density ratio depends on temperature. Finally, we obtain $v_{ns}$ from (1.2), that is, we set the counterflow velocity magnitude equal to $v_n + v_s$. Note that the $v_n$ values obtained from (1.1) by using the experimental volume cross-section, reported in table 1, are of the same order of (and consistently smaller than) the values of normal fluid velocity listed in table 2, with the largest relative difference observed for data set #2 and approximately equal to 50 % (the same applies when one compares the corresponding counterflow velocities).

Additionally, we can now calculate the scale $s_p$ probed by our particles and, to this end, we set $t_p = 5/f$ in (1.3) because, as discussed in § 2, the time resolution imposed by the chosen velocity estimation algorithm is equal to approximately $5\tau$, where $\tau = 1/f$. We can also compute the mean distance $s_q$ between quantized vortices from (1.4) by using the $v_{ns}$

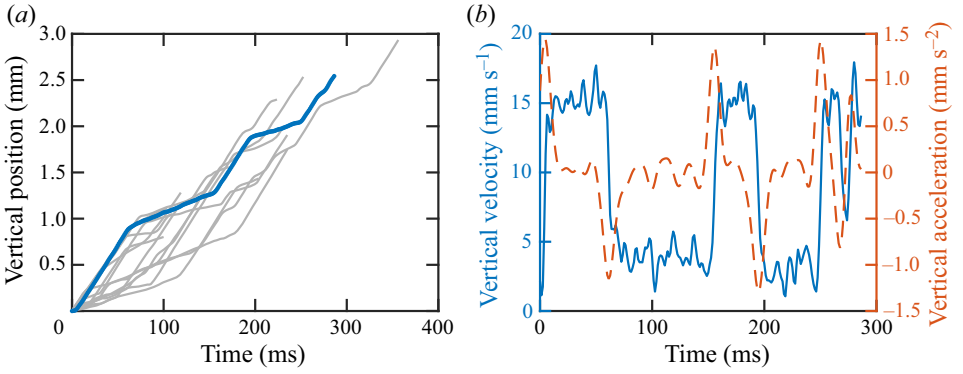


Figure 6. (*a*) Typical particle trajectories collected from data set #2. (*b*) Vertical velocity (blue solid line) and acceleration (red dashed line) of the particle track highlighted in panel (*a*).

values listed in table 2, that is, those derived from the statistical distributions of the particle vertical velocity – relevant $\gamma$ values were obtained following Švančara *et al.* (2018*b*). The scales estimated in such a way are also reported in table 2, together with the corresponding ratio $R$.

We find that, for the chosen data sets, the smallest resolved scale is of the same order of the mean distance between quantized vortices. The outcome does not change appreciably, if, for the estimation of $s_q$, we employ the thermal counterflow velocities derived from (1.2) by using the experimental volume cross-section, see table 1. Indeed, the obtained $R$ values are still of order one, although slightly smaller than those listed in table 2, that is, the corresponding scale ratios are equal to 1.5, 0.5 and 1.8 for data sets #1, #2 and #3, respectively.

It then follows that, for the present statistical distributions of the particle velocity, the most significant deviations from the Gaussian shape should be observed for data set #2. This is indeed the case, as shown in figure 4. The outcome is consistent with the fact, mentioned in § 1, that neat power-law tails are usually observed solely for $R$ values appreciably smaller than 1.

### 3.2. *Bimodal dynamics and trajectory segmentation*

A striking observation of this paper is apparent from the time evolution of the vertical position of some particles, see figure 6(*a*). Two characteristic slopes can be easily spotted, corresponding to the peak velocities $v_1$ and $v_2$. Let us follow the highlighted trajectory. We plot its vertical velocity and acceleration as a function of time in figure 6(*b*). Note that rapid velocity changes between two roughly constant values are clearly visible and consistent with the corresponding acceleration changes.

The behaviour allows us to develop a separation scheme in the velocity–acceleration phase space, shown in figure 7 for data set #2. The trajectory highlighted in figure 6 takes the form of several loops (white points) and the areas of higher density of points, near the line of zero acceleration, represent the two peak velocities (note the bivariate p.d.f. plotted as the colour-coded background).

Our separation scheme is based on that developed by Mastracci & Guo (2018), but, while they separated motion regimes solely on the basis of the particle vertical velocity, here we divide the two-dimensional phase space into four subspaces (or motion types), labelled throughout the paper as slow ($S$), fast ($F$), acceleration ($A$) and deceleration ($D$).

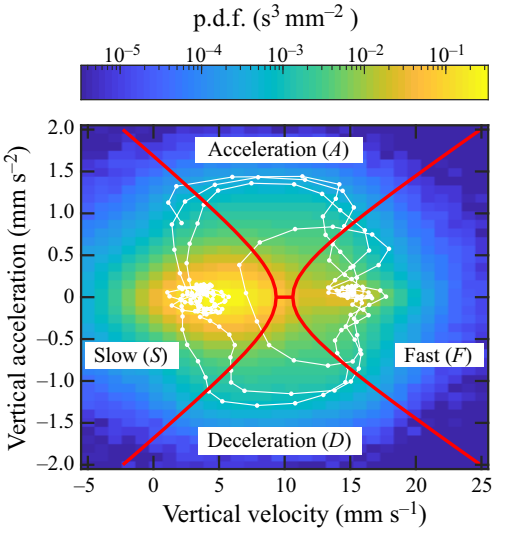


Figure 7. Separation scheme for data set #2. Colour-coded map: bivariate p.d.f. of the measured velocity–acceleration pairs. White points, trajectory highlighted in figure 6. Two hyperbolas and a segment (red lines) divide the phase space into four motion types, see the text for details.

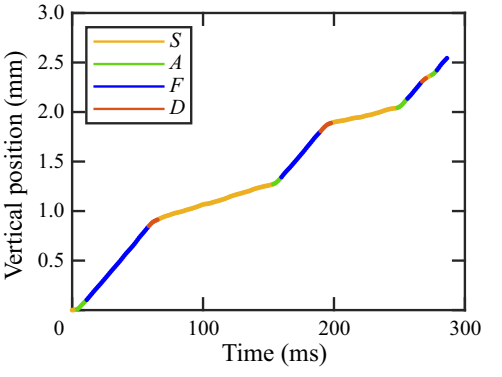


Figure 8. Trajectory highlighted in figure 6 separated into segments according to the scheme discussed in the text.

We define the respective separating curves as: (i) a slow hyperbola, with focus in $[v_1, 0]$ and semi axes of lengths $2\sigma(v_1)$ and $2\sigma(a_y)$; (ii) a fast hyperbola, with focus in $[v_2, 0]$ and semi axes of lengths $2\sigma(v_2)$ and $2\sigma(a_y)$; and (iii) a segment between the points $[v_1 + 2\sigma(v_1), 0]$ and $[v_2 - 2\sigma(v_2), 0]$. The values $v_i$ and $\sigma(v_i)$, with $i \in \{1, 2\}$, are obtained from Gaussian fits, and $\sigma(a_y)$ denotes the standard deviation of the particle vertical acceleration (its mean value is very close to zero in all considered cases). These curves are plotted as thick red lines in figure 7.

The segmentation of the exemplary trajectory, plotted in figure 8, indicates that the proposed scheme correctly identifies different motion regimes and can be used to split other trajectories. Note that spurious short segments of type $A$ or $D$, consisting of fewer than three points, are sometimes observed in the segmentation scheme results. They usually precede and follow much longer segments of type $S$ or $F$, and most likely indicate false transitions between regimes of the same type, that is, they are due to the noise level of the computed particle acceleration. In order to prevent excessive trajectory fragmentation,

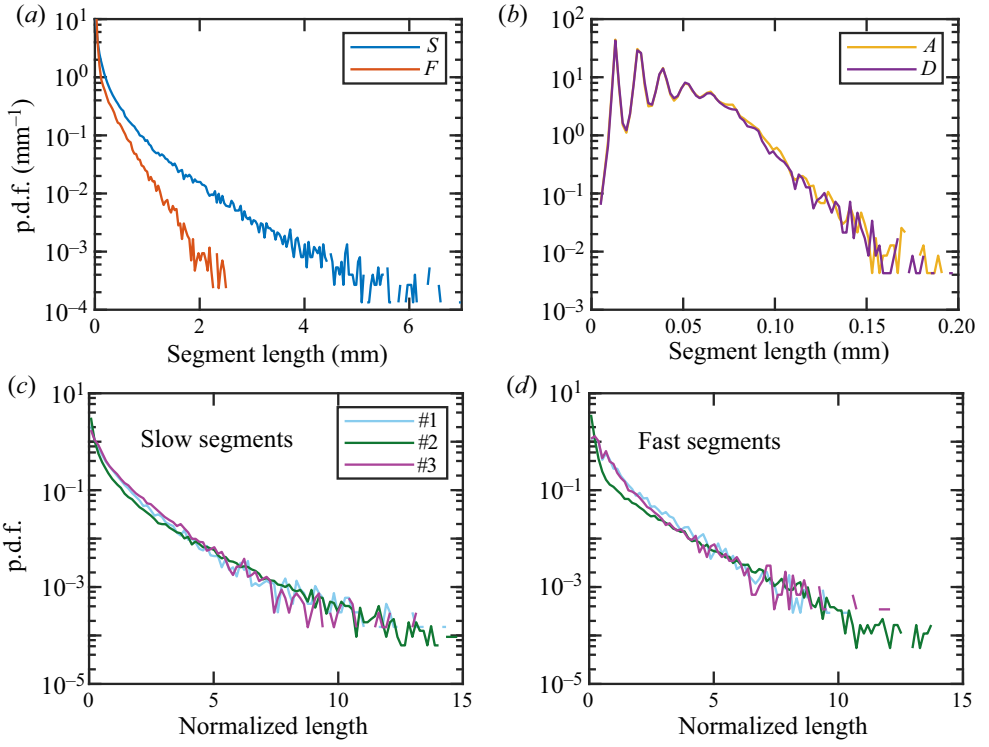


Figure 9. The p.d.f.s of segment lengths. (*a*,*b*) The p.d.f.s of different types obtained from data set #2. (*c*,*d*) Comparison of different data sets; lengths are here normalized by their standard deviations. The segment type is specified in panels (*a*–*d*).

| # | $\mu_S$ (μm) | $\sigma_S$ (μm) | $\mu_F$ (μm) | $\sigma_F$ (μm) |
|---|---|---|---|---|
| 1 | 279 | 425 | 108 | 137 |
| 2 | 221 | 415 | 86 | 178 |
| 3 | 90 | 123 | 170 | 230 |

Table 3. Characteristic lengths of trajectory segments; $\mu$, mean; $\sigma$, standard deviation. The subscripts $S$ and $F$ denote slow and fast trajectory segments, respectively; see the text for details.

we decided to merge these short segments with their respective neighbours. This choice led to the softening of the separation scheme, but, at the same time, it helped to retrieve long segments of type $S$ or $F$, which are discussed in the following section.

### 3.3. *Segment length distributions*

We define the segment length as the physical distance separating its first and last point (segments consisting of a single point have zero length). Typical distributions of segment lengths of different types are plotted in figure 9(*a*,*b*). Although the p.d.f.s of slow and fast segments (figure 9*a*) are highly peaked near zero, we see that the distributions are fairly broad and segments of lengths appreciably exceeding the mean distance between quantized vortices, approximately 0.06 mm for the displayed data set, are relatively common. We summarize the mean values and standard deviations of segment lengths in table 3.

The lengths of segments of type $F$, associated with fast particles, indicate that the latter can often travel long distances without changing their motion regime, i.e. without being significantly disturbed by quantized vortices during their upward journey. The outcome suggests therefore that the vortex tangle is likely not uniformly distributed in the considered flow region; this, by the way, is consistent with our current understanding of counterflow in vertical channels – see, for example, Švančara *et al.* (2018*b*) and Varga & Skrbek (2019). Note also that Kivotides (2008*b*) observed a similar depletion of particle–vortex interactions in relevant numerical simulations.

The length distributions obtained in different conditions collapse if we normalize the segment length by its standard deviation, see figure 9(*c*,*d*). This may indicate that the distribution shape is not significantly influenced by the vortex line density. However, we do not observe any clear relation between the mean segment length and the mean distance between quantized vortices.

The lengths of transition segments – $A$ and $D$, see figure 9(*b*) – display much narrower p.d.f.s, with typical lengths comparable to the mean distance $s_q$ between quantized vortices. It is very tempting to conclude that these abrupt events of large acceleration (deceleration) occur in the vicinity of quantized vortices, but, unfortunately, the time resolution of the present measurements does not allow such a strong claim. Indeed, we mentioned in § 2 that the effective time resolution of our acceleration measurements is appreciably larger than that of the velocity estimates. It then follows that the former scale ratios are approximately three times larger than the latter ones, which are reported in table 2. Our results therefore suggest that the observed events of large acceleration (deceleration) may occur in the proximity of quantized vortices, but, in order to make a stronger statement, we would need to access smaller scales, i.e. to improve our time resolution, which, by the way, is technically feasible (see, for example, Voth *et al.* 2002). Note also that the oscillations seen in this panel at small length are an experimental artefact, due to the finite camera frame rate, because the individual peaks represent the contributions of trajectory segments containing the same number of particle positions.

### 3.4. *Conditioned velocity distributions*

The p.d.f.s of vertical and horizontal velocities, obtained from data set #2, are plotted in figure 10(*a*,*b*). While the grey points indicate the unconditioned p.d.f.s, scaled to unit area, the colour lines denote the respective contributions of different motion types (types $A$ and $D$ are merged together, for the sake of clarity). Note that all the physical velocities are normalized by the standard deviation of the unconditioned data and that the areas under the p.d.f.s reflect the relative abundance of individual motion types.

The p.d.f.s of the particle vertical velocity (figure 10*a*) clearly show that motion types $S$ and $F$ are well separated (the small overlap is due to the removal of very short segments, mentioned above). For the p.d.f.s in the horizontal direction, displayed in figure 10(*b*), we observe that, at large enough velocities, the distributions of all motion types neatly deviate from the Gaussian shape, displayed as the black dashed line. The trends for all the three data sets considered here are displayed in figure 10(*c*,*d*), where we plot the p.d.f.s conditioned by the motion type $S$ (figure 10*c*) and $F$ (figure 10*d*). Note that shapes close to the Gaussian one are observed only for data set #3, which is characterized by the largest ratio between the scale probed by the particles and the quantum scale, see table 2.

This result contradicts the findings of Mastracci & Guo (2018). They reported that the horizontal velocity distributions of particles belonging to their group $G2$, loosely corresponding to our motion type $F$, strictly display a Gaussian form. Based on this observation, they claimed that these particles behave as if the vortex tangle were absent,

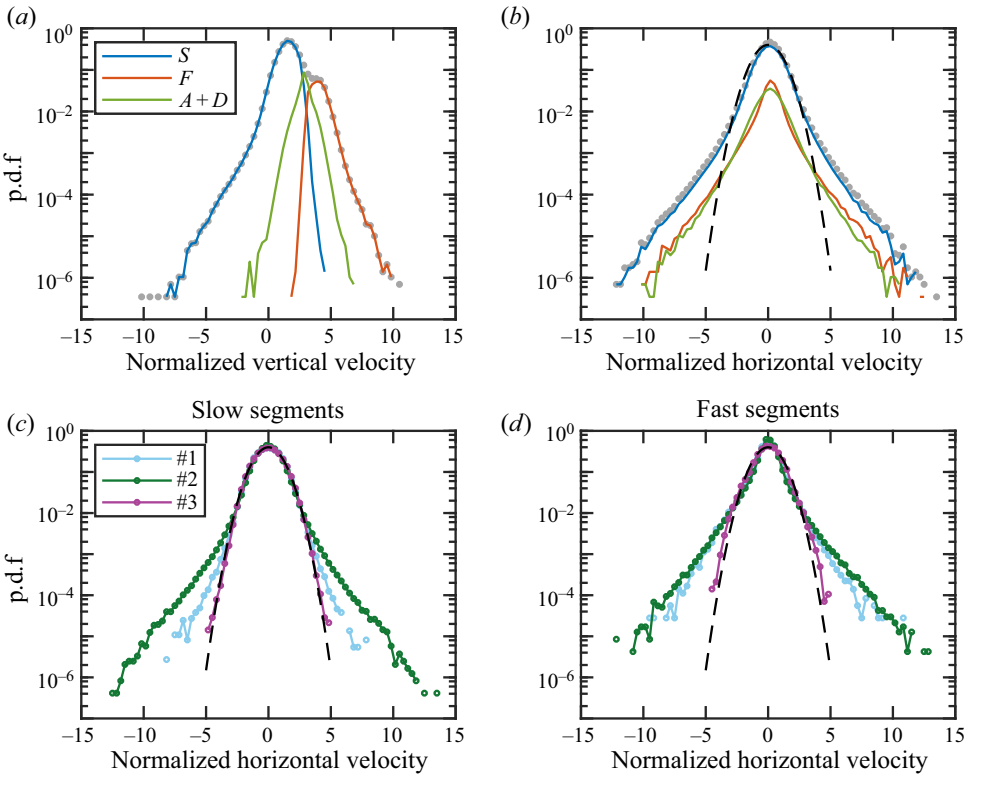


Figure 10. The p.d.f.s of Cartesian velocities, conditioned by the motion regime. (*a*,*b*) The p.d.f.s of the horizontal and vertical components obtained from data set #2 ($A + D$ corresponds to the merged data of types $A$ and $D$); grey points denote unconditioned velocity distributions, scaled to unit area (dimensional velocities are normalized by using the standard deviation of unconditioned data). Black dashed line, Gaussian distribution. (*c*,*d*) The p.d.f.s of the horizontal component obtained from the chosen data sets and conditioned by segments of types $S$ and $F$; all distributions are scaled to unit area.

but our results suggest a different physical picture, that is, both fast and slow particles appear to interact with the vortex tangle, at least in the range of investigated parameters – several arguments supporting the close relation between velocity distribution heavy tails and particle–vortex interactions are presented by La Mantia *et al.* (2016). Additionally, the latter interactions could be influenced by the the normal fluid vortical structures observed in numerical simulations (Idowu *et al.* 2000; Yui *et al.* 2020), in the close proximity of moving quantized vortices. However, these wake structures were observed at relatively small fluid velocities, that is, their topology in dense vortex tangles, which are specifically relevant for the present study, is currently unknown.

The disagreement between our measurements and those reported by Mastracci & Guo (2018) is most likely due to the relatively small sizes of the data sets they discussed, which are at least one order of magnitude smaller than ours – this is apparent if one compares p.d.f.s plotted in logarithmic–linear scale – and which consequently do not allow us to resolve events of large velocity occurring at small scales and with much smaller probability.

Mastracci & Guo (2018) also reported velocity fluctuations of particles belonging to their group $G2$ – fast particles – and, consistently with the corresponding velocity distribution shapes, these fluctuations were interpreted solely as an effect of the normal

fluid flow on the particle dynamics, see also Mastracci *et al.* (2019). They specifically found that horizontal and vertical velocity fluctuations of fast particles are qualitatively different, with the latter larger than the former, but this is not apparent from our data, that is, we do not see any consistent dependence of velocity fluctuations on experimental parameters. This might be related once more to the relatively small size of the data sets collected in the past and/or to the fact that these studies were performed at relatively small heat fluxes (Yui *et al.* 2020).

We may therefore say that, at sufficiently large heat fluxes, particle–vortex interactions cannot be neglected, but this could possibly be the case at heat fluxes smaller than those considered in the present study, that is, in the laminar regime for the normal fluid component. Additionally, as shown in the following section, the particle trajectories for motion types $S$ and $F$ appear to have different topologies, that is, the strength of the corresponding particle–vortex interactions does not seem to be the same in the two cases.

### 3.5. *Distributions of the velocity orientation angle*

The idea of different interaction strengths came to us from studying the appearance of the particle trajectories. We observed that segments of type $F$ are considerably straighter than those of type $S$ and, additionally, we found similar observations in the literature (Chagovets & Van Sciver 2011; La Mantia 2016). It was specifically argued that the erratic, wiggly paths of some particles may be related to frequent interactions between the particles and quantized vortices. In contrast, fast particles are expected to follow the more uniform flow field of the normal component. Here, we study the behaviour quantitatively, by evaluating how straight the individual trajectory segments are, focusing mostly on motion types $S$ and $F$.

In order to quantify the trajectory shape, we employ the velocity orientation angle $\theta$, which can be evaluated along the trajectory, for each point, and is defined, following Paoletti *et al.* (2008), as

$$\theta = \arctan\left(\frac{v_y}{v_x}\right), \tag{3.3}$$

where $v_y$ and $v_x$ indicate the particle velocities in the vertical and horizontal directions, respectively. Note that $\theta$ can be evaluated in the full angular range, yielding values $-\pi \leq \theta \leq \pi$. The direction of the normal fluid flow corresponds to $\theta = \pi/2$ and that of the superflow to $\theta = -\pi/2$.

We plot the p.d.f.s of the unconditioned orientation angle in figure 11($a$), where we compare the distributions obtained in thermal counterflow with a control data set measured when the heater was switched off (red line). We observe that the latter distribution is relatively constant, indicating that the corresponding velocity vectors do not have a preferred orientation. The small equidistant peaks are experimental artefacts due to the finite spatial resolution, almost equivalent to the bias known as peak-locking in particle imaging velocimetry (Raffel *et al.* 2018). Indeed, it is impossible to achieve subpixel resolution with a one-pixel particle. Therefore this particle will move to one of the eight pixels around it in the next frame (the average velocity being zero in this case), and induce a small bias for $\theta$, equal to $\pi/4$. Instead, in thermal counterflow, we observe a strong preferential orientation of the velocity vectors in the direction of the normal component. This confirms that our data belongs to the intermediate range of counterflow velocity discussed in § 1 and, additionally, means that most particles follow relatively straight vertical trajectories.

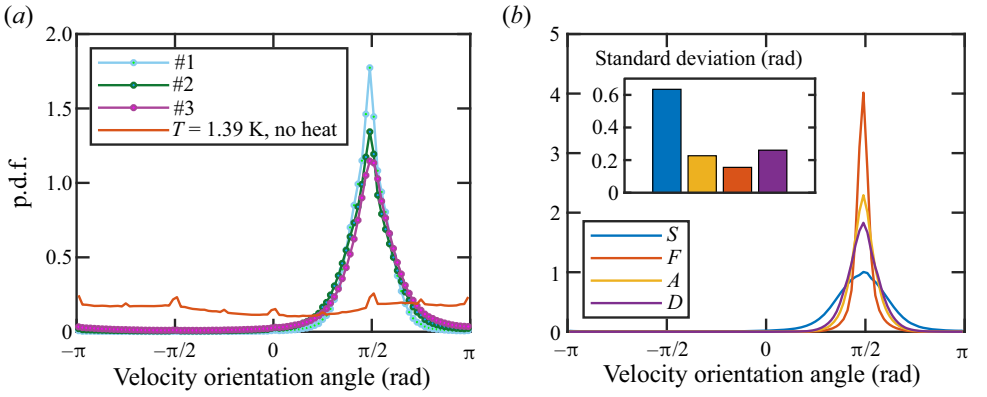


Figure 11. The p.d.f.s of the velocity orientation angle $\theta$, see (3.3). (*a*) Comparison of the chosen data sets with a residual flow with no applied heat flux. (*b*) The p.d.f.s corresponding to the individual motion types, from data set #2; inset: standard deviation of the distributions, displayed in the order corresponding to a typical time evolution of particle motion, that is, $S \rightarrow A \rightarrow F \rightarrow D$.

Deviations from straight trajectories, that is, particle tracks with constant $\theta$, can be quantified by using the width of the corresponding distribution peaks. We plot p.d.f.s of different motion types in figure 11(*b*), and, as expected, segments of type $S$ display a significantly broader distribution – i.e. of larger standard deviation (see inset) – than that of type $F$. The result indicates not only that slow particles are, on average, slower than fast ones but also that their trajectories are subjected to larger deviations, as they seem to strongly interact with nearby vortices.

### 3.6. *Particle accelerations*

A number of previous experimental studies (La Mantia *et al.* 2013; La Mantia & Skrbek 2014; La Mantia 2017; Švančara & La Mantia 2017) showed that information obtained from the accelerations of particles probing turbulent flows of superfluid $^4$He may contribute to our understating of the underlying physics. It was reported, for example, that the statistical distributions of the particle acceleration display classical-like shapes at sufficiently large scales, regardless of the flow type (La Mantia *et al.* 2013; Švančara & La Mantia 2017) and of the boundary proximity (La Mantia 2017). Additionally, experimentally obtained mean values of the particle acceleration were used to test relevant models of particle dynamics, taking especially into account added mass effects (La Mantia *et al.* 2013; La Mantia & Skrbek 2014).

Similarly, the present results suggest that not only particle velocities but also their accelerations may give useful information for the identification of the two motion regimes corresponding to fast and slow particles. However, the works just mentioned (La Mantia *et al.* 2013; La Mantia & Skrbek 2014; La Mantia 2017; Švančara & La Mantia 2017) focused on general features of the observed particle dynamics, that is, they were less concerned by the investigation of single particle trajectories, which is instead the focus of the present study. We therefore decided to employ here the smoothing scheme described in § 2, considering that one should be aware that experimental noise – due, for example, to the imprecise location of the particles – can be greatly amplified by common differentiation schemes, especially in the case of accelerations, usually computed as the second time derivative of the particle positions (see, for example, Voth *et al.* 2002; Lawson *et al.* 2018).

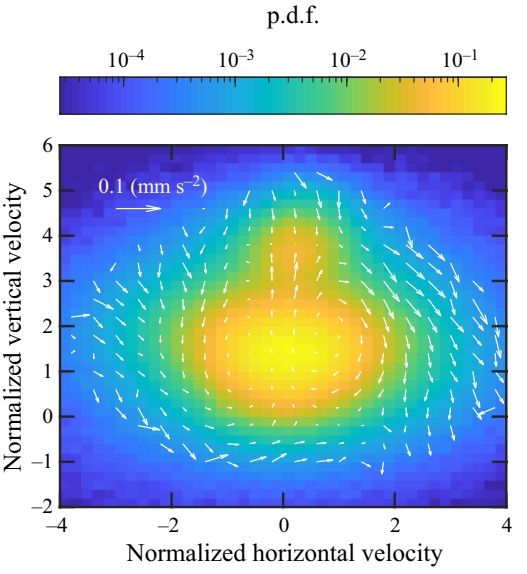


Figure 12. Mean particle acceleration conditioned by the particle velocity. Colour map: bivariate p.d.f. of the particle velocity; both velocity components are normalized by their standard deviations. White arrows, mean acceleration map; accelerations are computed on a mesh two times coarser than the velocity p.d.f. and are shown only if the corresponding bin counts more than 500 samples. The results are obtained from data set #2.

The drawback of our choice is the loss of time resolution in comparison with the data processing schemes used in the past, which, nevertheless, gave results consistent with the proposed physical description of the problem. Indeed, as mentioned above, the effective time resolution for the calculated accelerations is approximately three times larger than that associated with the particle velocities – note, for example, that the acceleration of the exemplary trajectory shown in figure 6 is a smoother function of time than the corresponding velocity. On the other hand, the advantage of our choice is that, in comparison with previous studies, we are confident that the chosen data processing scheme is less prone to noise amplification, that is, we believe that our separation scheme is robust enough to detect the occurrence of motion types $S$ and $F$.

The idea that acceleration estimates may be important for the present analysis can also be supported by the pattern of the mean particle acceleration, conditioned by both velocity components, displayed in figure 12. The mean acceleration is indicated in the figure by white arrows and the colour map shows the bivariate p.d.f. of the particle velocity. It seems that, on average, particles accelerate, that is, break free from the slow state and start to follow the normal component, when their horizontal velocity is close to zero. In contrast, we observe that events corresponding to particle deceleration in the vertical direction are coupled to non-zero horizontal velocity. It then appears that particle deceleration and acceleration events do not share the same features. The former events seem to be more abrupt than the latter, as they apparently increase the particle velocity in the direction perpendicular to the mean flow. Possibly, these events may be related to Kelvin waves generated on the vortex lines when particles are in their close proximity (Kivotides 2008*b*; Giuriato & Krstulovic 2019).

Additionally, from the figure it is apparent that the obtained mean accelerations are smaller than 0.1 mm s$^{-2}$. In order to physically interpret the latter value, one could start from the fact that the pressure gradient force, per unit of mass, attracting a spherical

particle to a quantized vortex core is proportional to $\kappa^2/d^3$, where $d$ indicates the distance between the particle and vortex core – see, for example, La Mantia *et al.* (2013) for the exact expression. A pressure gradient force of $0.1\ \mathrm{mm\,s^{-2}}$ is obtained for a distance equal to approximately 120 $\mu$m, which is comparable to the scale probed by our particles, approximately 150 $\mu$m in the case of accelerations. On the other hand, if we set $d = 50\ \mu$m, which is comparable to the estimated quantum scale $s_q$, see table 2, we find that the pressure gradient force is $1.5\ \mathrm{mm\,s^{-2}}$, a value much larger than the mean accelerations shown in figure 12, but of the same order of the peak accelerations displayed in figure 6.

The reader should, nevertheless, keep in mind that the latter considerations on particle accelerations are rather speculative mainly because no obvious pattern in this phase space was observed for individual trajectories. Additionally, other experimental conditions should be investigated and data sets appreciably larger than the present ones should be collected. A clearer picture may also be achieved with better time resolution, which can be obtained, for example, with higher camera frame rates, i.e. by reducing the scale probed by the particles. Indeed, precise measurements of particle acceleration were achieved in classical flows with very fast pixel detectors originally developed for high energy physics (Voth *et al.* 2002; Mordant *et al.* 2004).

## 4. Conclusions

The behaviour of relatively small solid particles displays multiple regimes in thermal counterflow of superfluid $^4$He. Within the investigated range of experimental parameters, we observe a clear bimodal dynamics along particle trajectories. These two regimes can be associated with fast particles, moving in the direction of the normal fluid along almost straight tracks, and to slow particles, whose erratic upward motion appears to be significantly influenced by quantized vortices. The regimes, together with the corresponding transition events, were identified by using a custom-made separation scheme, based on the identification of specific trajectory patterns in the two-dimensional velocity–acceleration phase space. It is important to stress that a single particle can explore both regimes during its motion away from the heat source.

Particle trajectories, split into individual segments according to the motion regimes, were then studied separately. We observed the occurrence of very long segments, meaning that particles can be fast or slow on macroscopic length scales, appreciably larger than the mean distance between quantized vortices. We found that fast particles move, on average, with velocities close to the normal fluid velocity $v_n$, once the density mismatch between particle and fluid is accounted for, and that the trajectories of these particles are relatively straight. The slow particles seem instead to be influenced by stronger interactions with the vortex tangle. Their mean velocity is reduced to approximately $v_n/2$ and their tracks are considerably more erratic. We also observed that the particle velocity p.d.f.s reveal extreme events (heavy tails) in both cases but with different strengths that may be related to their different interaction with the underlying vortex tangle.

It then follows that the interactions between quantized vortices and flow-probing particles are ubiquitous in thermal counterflow of superfluid helium. They appear to be relevant not only for the slow particles, as claimed in the past, for example, by Mastracci & Guo (2018), but also for the fast ones, at least at sufficiently large heat fluxes, in turbulent counterflow. This can be regarded as the work's main scientific result, obtained by applying the proposed separation scheme.

In summary, we believe that this work not only makes a significant contribution to our current understanding of particle–vortex interactions in quantum turbulence, but also

presents a data processing scheme that could be used to interpret particle dynamics in other flows. Additionally, retrieving patterns in the four-dimensional velocity–acceleration phase space, as outlined in § 3.6, may be useful for the neat identification of particle deceleration and acceleration events, that is, to study the still largely unknown dynamics of particles trapped onto quantized vortices, once adequate time resolution is achieved. We also envisage that these patterns could be detected by using contemporary computational methods, such as neural networks and machine learning, following, for example, Dosset *et al.* (2016), and that seeking similar behavioural patterns in numerical simulations could also be a feasible line of future research, if one considers, for example, the recent work by Polanco & Krstulovic (2020).

**Funding.** The visits to Prague of P.D., B.R., M.B. and M.G. were supported by the EuHIT project QuantumPC. The visits to Grenoble of P.Š. and D.D. were supported by the French Barrande program, the Czech Mobility program, the Charles University Mobility Fund and the Czech Science Foundation. The latter also supported the experiments discussed here. M.G. acknowledges the support of grants ANR-11-PDOC-0001 (3D-QuantumV) and ANR-10-LABX-0051 (LANEF). P.Š., M.R., L.S. and M.L.M. acknowledge the support of the Czech Science Foundation (GAČR) under grant no. 19-00939S.

**Declaration of interests.** The authors report no conflict of interest.

**Author ORCIDs.**
P. Švančara http://orcid.org/0000-0001-7285-6332;
M. Rotter http://orcid.org/0000-0001-6779-179X;
L. Skrbek http://orcid.org/0000-0002-6016-1194;
M. La Mantia http://orcid.org/0000-0002-7159-5924;
P. Diribarne http://orcid.org/0000-0002-9772-9097;
B. Rousset http://orcid.org/0000-0002-0340-1243;
M. Bourgoin http://orcid.org/0000-0001-9442-7694;
M. Gibert http://orcid.org/0000-0002-5248-492X.

## References

Babuin, S., Stammeier, M., Varga, E., Rotter, M. & Skrbek, L. 2012 Quantum turbulence of bellows-driven $^4$He superflow: steady state. *Phys. Rev.* B **86**, 134515.

Baggaley, A.W. & Laizet, S. 2013 Vortex line density in counterflowing He II with laminar and turbulent normal fluid velocity profiles. *Phys. Fluids* **25**, 115101.

Barenghi, C.F., Skrbek, L. & Sreenivasan, K.R. 2014 Introduction to quantum turbulence. *Proc. Natl Acad. Sci. USA* **111**, 4647–4652.

Bertolaccini, J., Lévêque, E. & Roche, P.-E. 2017 Disproportionate entrance length in superfluid flows and the puzzle of counterflow instabilities. *Phys. Rev. Fluids* **2**, 123902.

Bostanjoglo, O. & Kleinschmidt, R. 1967 Crystal structure of hydrogen isotopes. *J. Chem. Phys.* **46**, 2004–2005.

Chagovets, T.V. & Van Sciver, S.W. 2011 A study of thermal counterflow using particle tracking velocimetry. *Phys. Fluids* **23**, 107102.

Donnelly, R.J. & Barenghi, C.F. 1998 The observed properties of liquid helium at the saturated vapor pressure. *J. Phys. Chem. Ref. Data* **27**, 1217–1274.

Dosset, P., Rassam, P., Fernandez, L., Espenel, C., Rubinstein, E., Margeat, E. & Milhiet, P.-E. 2016 Automatic detection of diffusion modes within biological membranes using back-propagation neural network. *BMC Bioinform.* **17**, 197.

Giuriato, U. & Krstulovic, G. 2019 Interaction between active particles and quantum vortices leading to Kelvin wave generation. *Sci. Rep.* **9**, 4839.

Guo, W., La Mantia, M., Lathrop, D.P. & Van Sciver, S.W. 2014 Visualization of two-fluid flows of superfluid helium-4. *Proc. Natl Acad. Sci. USA* **111**, 4653–4658.

Hrubcová, P., Švančara, P. & La Mantia, M. 2018 Vorticity enhancement in thermal counterflow of superfluid helium. *Phys. Rev.* B **97**, 064512.

IDOWU, O.C., WILLIS, A., BARENGHI, C.F. & SAMUELS, D.C. 2000 Local normal-fluid helium II flow due to mutual friction interaction with the superfluid. *Phys. Rev.* B **62**, 3409–3415.

KIVOTIDES, D. 2008*a* Motion of a spherical solid particle in thermal counterflow turbulence. *Phys. Rev.* B **77**, 174508.

KIVOTIDES, D. 2008*b* Normal-fluid velocity measurement and superfluid vortex detection in thermal counterflow turbulence. *Phys. Rev.* B **78**, 224501.

LA MANTIA, M. 2016 Particle trajectories in thermal counterflow of superfluid helium in a wide channel of square cross section. *Phys. Fluids* **28**, 024102.

LA MANTIA, M. 2017 Particle dynamics in wall-bounded thermal counterflow of superfluid helium. *Phys. Fluids* **29**, 065102.

LA MANTIA, M., DUDA, D., ROTTER, M. & SKRBEK, L. 2013 Lagrangian accelerations of particles in superfluid turbulence. *J. Fluid Mech.* **717**, R9.

LA MANTIA, M. & SKRBEK, L. 2014 Quantum turbulence visualized by particle dynamics. *Phys. Rev.* B **90**, 014519.

LA MANTIA, M., ŠVANČARA, P., DUDA, D. & SKRBEK, L. 2016 Small-scale universality of particle dynamics in quantum turbulence. *Phys. Rev.* B **94**, 184512.

LAWSON, J.M., BODENSCHATZ, E., LALESCU, C.C. & WILCZEK, M. 2018 Bias in particle tracking acceleration measurement. *Exp. Fluids* **59**, 172.

MASTRACCI, B., BAO, S., GUO, W. & VINEN, W.F. 2019 Particle tracking velocimetry applied to thermal counterflow in superfluid $^4$He: motion of the normal fluid at small heat fluxes. *Phys. Rev. Fluids* **4**, 083305.

MASTRACCI, B. & GUO, W. 2018 Exploration of thermal counterflow in He II using particle tracking velocimetry. *Phys. Rev. Fluids* **3**, 063304.

MONGIOVÌ, M.S., JOU, D. & SCIACCA, M. 2018 Non-equilibrium thermodynamics, heat transport and thermal waves in laminar and turbulent superfluid helium. *Phys. Rep.* **726**, 1–71.

MORDANT, N., CRAWFORD, A.M. & BODENSCHATZ, E. 2004 Experimental Lagrangian acceleration probability density function measurement. *Physica* D **193**, 245–251.

PAOLETTI, M.S., FIORITO, R.B., SREENIVASAN, K.R. & LATHROP, D.P. 2008 Visualization of superfluid helium flow. *J. Phys. Soc. Japan* **77**, 111007.

POLANCO, J.I. & KRSTULOVIC, G. 2020 Inhomogeneous distribution of particles in coflow and counterflow quantum turbulence. *Phys. Rev. Fluids* **5**, 032601(R).

RAFFEL, M., WILLERT, C.E., SCARANO, F., KÄHLER, C.J., WERELEY, S.T. & KOMPENHANS, J. 2018 *Particle Image Velocimetry – A Pratical Guide*. Springer.

SERGEEV, Y.A. & BARENGHI, C.F. 2009 Particles-vortex interactions and flow visualization in $^4$He. *J. Low Temp. Phys.* **157**, 429–475.

SERGEEV, Y.A., BARENGHI, C.F. & KIVOTIDES, D. 2006 Motion of micron-size particles in turbulent helium II. *Phys. Rev.* B **74**, 184506.

SKRBEK, L. & SREENIVASAN, K.R. 2012 Developed quantum turbulence and its decay. *Phys. Fluids* **24**, 011301.

ŠVANČARA, P., HRUBCOVÁ, P. & LA MANTIA, M. 2018*a* Estimation of Lagrangian velocities in thermal counterflow of superfluid helium by a multi-point algorithm. In *WDS'18 Proceedings of Contributed Papers – Physics* (ed. J. Pavlů & J. Šafránková), pp. 168–173. MatfyzPress.

ŠVANČARA, P., HRUBCOVÁ, P., ROTTER, M. & LA MANTIA, M. 2018*b* Visualization study of thermal counterflow of superfluid helium in the proximity of the heat source by using solid deuterium hydride particles. *Phys. Rev. Fluids* **3**, 114701.

ŠVANČARA, P. & LA MANTIA, M. 2017 Flows of liquid $^4$He due to oscillating grids. *J. Fluid Mech.* **832**, 578–599.

ŠVANČARA, P. & LA MANTIA, M. 2019 Flight-crash events in superfluid turbulence. *J. Fluid Mech.* **876**, R2.

VARGA, E. & SKRBEK, L. 2019 Thermal counterflow of superfluid $^4$He: temperature gradient in the bulk and in the vicinity of heater. *Phys. Rev.* B **100**, 054518.

VOTH, G.A., LA PORTA, A., CRAWFORD, A.M. & BODENSCHATZ, E. 2002 Measurement of particle accelerations in fully developed turbulence. *J. Fluid Mech.* **469**, 121–160.

YUI, S., KOBAYASHI, H., TSUBOTA, M. & GUO, W. 2020 Fully coupled two-fluid dynamics in superfluid $^4$He: anomalous anisotropic velocity fluctuations in counterflow. *Phys. Rev. Lett.* **124**, 155301.

ZHANG, T. & VAN SCIVER, S.W. 2005 The motion of micron-sized particles in He II counterflow as observed by the PIV technique. *J. Low Temp. Phys.* **138**, 865–870.